Journal of Physics:
Conference Series

PURPOSE-LED
PUBLISHING™

PAPER • **OPEN ACCESS**

Characterisation of rough-wall drag in compressible turbulent boundary layers

To cite this article: D. D. Wangsawijaya *et al* 2026 *J. Phys.: Conf. Ser.* **3173** 012023

View the article online for updates and enhancements.

You may also like

- By-pass transition of flat plate boundary layers on the surfaces near the limit of admissible roughness
P Jonáš, O Hladík, O Mazur et al.
- Similarity of instantaneous and filtered velocity fields in the near wall region of zero-pressure gradient boundary layer
Akihiko Nakayama, Hiroshi Noda and Kazuhiro Maeda
- Turbulence structure in boundary layers over different types of surface roughness
R A Antonia and P-Å Krogstad

Journal of Physics: Conference Series **3173** (2026) 012023 doi:10.1088/1742-6596/3173/1/012023

Characterisation of rough-wall drag in compressible turbulent boundary layers

D. D. Wangsawijaya[1], R. Baidya[2,3], S. Scharnowski[2], B. Ganapathisubramani[1], and C. J. Kähler[2]

[1]University of Southampton, University Road SO17 1BJ, United Kingdom
[2]University of the Bundeswehr Munich, Werner-Heisenberg-Weg 39, 85577 Neubiberg, Germany
[3]University of Melbourne, Grattan Street, Parkville VIC 3010, Australia

E-mail: D.D.Wangsawijaya@soton.ac.uk

Abstract. This study explores the possibility of transferring the established framework for drag characterisation in incompressible flow regime to that of the compressible flow regime, using the Hama roughness function ΔU^+ [1] and the equivalent sand grain roughness k_s [2]. Experiments are conducted for turbulent boundary layers (TBLs) developing over two types of sandpaper rough walls (P60- and P24-grit) across a Mach number range of $0.3 \geq M \geq 2.9$ to span the incompressible and compressible flow regime. Results suggest that the momentum deficit ΔU^+ is relatively independent of transformations to account for compressibility effects, while there seems to be a proportional shift from the ΔU^+ vs. $\log(k_s)$ incompressible relation with increasing M even in the fully rough regime. Thus, to be able to utilise the ΔU^+–k_s relation in incompressible flow regime, two empirical scaling factors are introduced. The first is a new roughness lengthscale $k_* = k/\nu_\infty^+$, where $\nu_\infty^+ = \nu_\infty/\nu_w$ is the freestream-to-wall kinematic viscosity ratio, while the second is a correction factor F_c, a function of freestream-to-wall temperature ratio T_∞/T_w, here utilised for the roughness function, $\sqrt{1/F_c}\Delta U^+$.

1 Introduction

In incompressible wall-bounded turbulent flows, drag penalty due to surface roughness is characterised by a log-law deficit from that of a smooth surface, corresponding to the Hama roughness function ΔU^+ [1],

$$U^+ = \frac{1}{\kappa}\log\left(y+d\right)^+ + B - \Delta U^+ \tag{1}$$

where κ is the von Kármán constant, $U^+ = U/U_\tau$ is the viscous-scaled mean streamwise velocity, U_τ is the friction velocity, $y^+ = yU_\tau/\nu$ is the viscous-scaled wall-normal coordinates, d is the zero-plane displacement, ν is the kinematic viscosity, and B is the log-law intercept. This study uses a constant $\kappa = 0.39$ and the log-law intercept $B = 4.3$, similar to those of [3, 4]. In the "fully rough" regime, ΔU^+ is solely a function of the equivalent sand-grain roughness k_s [2],

$$\Delta U^+ = \frac{1}{\kappa}\log k_s^+ + B - B_{FR} \tag{2}$$

where $k_s^+ = k_s U_\tau/\nu$ and $B_{FR} = 8.5$ is the fully rough intercept. The current framework for drag characterisation of incompressible, rough-wall turbulent boundary layers (TBLs) is well-established: ΔU^+

Content from this work may be used under the terms of the Creative Commons Attribution 4.0 licence. Any further distribution of this work must maintain attribution to the author(s) and the title of the work, journal citation and DOI.
Published under licence by IOP Publishing Ltd

Reference	Abbreviation	f_I	g_I
[5]	'VD'	1	$\rho^{+^{0.5}}$
[6]	'BR'	$\mu^{+^{-1}}$	$\left(\frac{\rho^+}{\mu^+}\right)^{0.5} \frac{y}{y_I}$
[7]	'TL'	$\frac{\mathrm{d}}{\mathrm{d}y}\left(\frac{y\rho^{+^{0.5}}}{\mu^+}\right)$	$\mu^+ \frac{\mathrm{d}}{\mathrm{d}y}\left(\frac{y\rho^{+^{0.5}}}{\mu^+}\right)$
[8]	'VO'	$\frac{\rho^{+^{0.5}}}{\mu^{+^{1.5}}}$	$\left(\frac{\rho^+}{\mu^+}\right)^{0.5}$

Table 1: Various transformation functions f_I and g_I related to equation (3), $\rho^+ \equiv \rho/\rho_w$ and $\mu^+ \equiv \mu/\mu_w$ are the density and dynamic viscosity profiles as a function of wall-normal coordinates, relative to the density and dynamic viscosity at the wall.

is obtained from flow measurements or simulations, and for a fully rough flow, k_s can be obtained directly from ΔU^+.

In the compressible flow regime, rough-wall TBLs comprise of phenomena related to high-speed flight vehicles, where the roughness (including steps and gaps) is likely to be induced during operations due to thermal expansion, ablation, dust impact, water and ice droplets. Here, the mean velocity profile U and wall-normal coordinate y of the TBL must be "stretched" to account for the compressibility effect. The generic form [8, 9] of U and y transformations to their incompressible equivalents, U_I and y_I, respectively, can be written as

$$y_I = \int_0^{\hat{y}} f_I(\hat{y})\, \mathrm{d}\hat{y} \quad \text{and} \quad U_I = \int_0^{\hat{U}} g_I(\hat{U})\, \mathrm{d}\hat{U} \tag{3}$$

where the functions f_I and g_I for different transformations are shown in table 1. These functions account for either density or viscosity variations across the boundary layer normalised by their values at the wall, here denoted by $\rho^+ = \rho/\rho_w$ and $\mu^+ = \mu/\mu_w$ (subscript 'w' denotes the value at the wall). The classical and the most well-known transformation, the Van Driest transformation (here abbreviated to 'VD') [5], for example, accounts for density variation from the derivation of the mean velocity gradient in the log-layer. Meanwhile, newer transformations have since attempted to improve the accuracy of the transformations: for specific wall conditions [7], or by utilising data-driven approach [8]. In addition to the VD transformation, 3 newer transformations are chosen for this study and listed in table 1: Brun, *et al.* ('BR') [6], Trettel & Larsson ('TL') [7], and Volpiani, *et al.* ('VO') [8].

For compressible, rough-wall TBLs, the current framework for drag characterisation is as follows: first, U and y are transformed into their incompressible equivalents, U_I and y_I. Then, the Hama roughness function is calculated from the stretched profile U_I, here denoted as ΔU_I^+. Finally, in the case of fully rough flow, k_s for a particular roughness is derived directly from its ΔU_I^+. This approach is evident in previous studies conducted on various types of roughnesses: 'sandpaper' [10, 11, 12], 'traverse bars' [13, 12, 14], 'sine waves' [15, 16], 'cubes' [12, 17, 9, 18], 'egg-carton' [16, 19], 'mesh' [14], and 'diamonds' [17, 20]. The majority of these studies were conducted in the supersonic regime, with some [14, 18, 19] extended towards the hypersonic regime.

Compared to the amount of data available for drag characterisation in the incompressible flow regime, there is much less data available in the compressible regime. Especially for experimental studies, k_s of a certain roughness was typically derived from a single Mach number M and Reynolds number Re measurement. Therefore, in this study, we investigate the possibility of transferring the established framework for rough-wall drag in incompressible flows to the compressible flow regime, i.e. by knowing the roughness parameter of a surface (such as k_s) for the incompressible flow case, can the behavior of the logarithmic region for the $M > 1$ cases be predicted? Measurement campaign is conducted for various sandpaper-type roughnesses in a range of M spanning subsonic, transonic, and supersonic flow regimes, and completed with an independent variation of Re at a constant M. The approach will be tested for various velocity transformations shown in table 1 to account for the compressibility effect.

2 Experimental set-up

2.1 Facility and test cases

Measurements are conducted for the TBLs developing over a 750 mm × 300 mm ($58\delta_0 \times 22\delta_0$, length × width) base flat plate installed inside the trisonic wind tunnel (TWM) at the University of the Bundeswehr

M [−]	M_∞ [−]	P_0 [bar]	T_0 [K]	T_∞/T_w [−]	U_∞ [m/s]	δ [mm]	Re_τ [−]	C_f [$\times 10^{-3}$]	Symbol VD	BR	TL	VO
Smooth Wall (SW)												
0.3	0.28	1.50	293	0.99	93.82	13.92	4355	2.53				
0.8	0.80	1.49	286	0.90	255.45	22.29	13361	2.11				
2.0	1.90	2.50	287	0.61	492.62	8.15	4140	1.73				
2.0	1.90	4.49	285	0.61	491.16	7.85	6933	1.60				
2.9	2.89	4.50	289	0.40	602.71	7.81	2233	1.50				
Rough Wall (P60)												
0.3	0.29	1.50	296	0.99	97.66	16.57	7427	4.95				
0.8	0.82	1.50	289	0.89	261.93	24.44	22391	4.97				
2.0	1.95	2.49	284	0.60	496.40	11.61	10446	5.82				
2.0	1.91	4.49	286	0.61	492.10	11.92	20271	5.99				
2.9	2.84	4.49	291	0.41	601.55	10.75	7812	8.93				
Rough Wall (P24)												
0.3	0.28	1.50	295	0.99	97.02	18.83	9830	6.74				
0.8	0.80	1.49	287	0.90	255.33	24.17	27025	7.42				
2.0	1.99	2.49	279	0.59	497.41	14.90	15594	8.11				
2.0	1.94	4.49	286	0.60	496.18	15.05	30292	8.89				
2.9	2.77	4.49	292	0.42	596.43	12.92	11167	10.82				

Table 2: List of test cases at a range of nominal test section Mach number M (the actual freestream Mach number M_∞ is obtained from PIV measurements). The freestream-to-wall temperature ratio is defined by T_∞/T_w, while δ is the 99% boundary-layer thickness measured at the stations marked by **A** and **B** in figure 1(a). The freestream Reynolds number $Re_\tau \equiv \delta U_\tau/\nu_w$ and the skin friction coefficient $C_f \equiv 2(\rho_w/\rho_\infty)(U_\tau/U_\infty)^2$ estimated from the profiles stretched by van Driest transformation [5]. Symbols mark various transformations shown in table 1, with lighter to darker colour schemes mark the lowest to highest Mach number test cases.

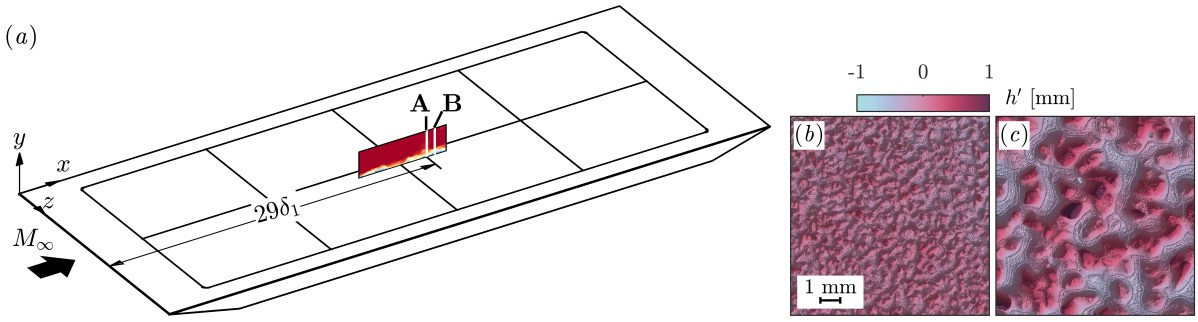


Figure 1: (a) The smooth flat plate with 8 inserts for the rough walls installations. The extent and position of the PIV (Particle Image Velocimetry) FOV (field-of-view) are shown. Label '**A**' marks the streamwise location of the velocity profiles used in the analysis for smooth wall (SW) and P24-grit rough wall cases, while '**B**' marks the location for P60-grit rough cases. Coloured contours of the deviation of sandpaper surface height from its mean, h', shown for 10 mm × 10 mm coupons of (b) P60- and (c) P24-grit sandpapers.

Param.	Unit	Formula	P60	P24
k	mm	$6\sqrt{\overline{h'^2}}$	0.595	1.695
k_a	mm	$\overline{\lvert h' \rvert}$	0.077	0.226
k_p	mm	$\max(h') - \min(h')$	0.804	2.023
k_{rms}	mm	$\sqrt{\overline{h'^2}}$	0.099	0.283
k_{sk}	–	$\overline{h'^3}/h_{rms}^3$	1.261	1.841
k_{ku}	–	$\overline{h'^4}/h_{rms}^4$	10.375	9.708
ES_x	–	$\overline{\lvert \frac{\mathrm{d}h'}{\mathrm{d}x} \rvert}$	0.541	0.659

Table 3: Key surface parameters from the scanned P60- and P24-grit sandpapers, h' is the surface deviation from its mean height, $h' = h - \overline{h}$.

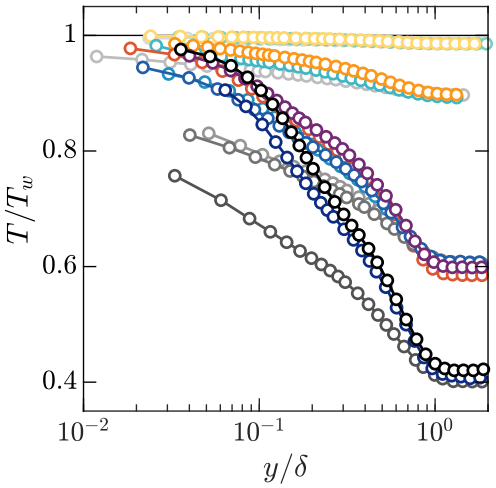


Figure 2: Temperature profile T/T_w as a function of wall-normal coordinates y/δ. Colours correspond to the test cases listed in table 2. Data are downsampled for clarity.

Munich, shown in figure 1(a). Here, δ_0 is the reference 99% smooth-wall boundary-layer thickness at a nominal test section Mach number $M = 0.3$. The base plate is equipped with 8 removable inserts, shown in figure 1(a), allowing multiple changes of test surfaces without removing the base plate from the test section.

Test surfaces comprise of a smooth wall ('SW') and two rough walls constructed from P60-and P24-grit sandpaper sheets, presented in the test matrix in table 2. Samples of P60- and P24-grit sandpapers are scanned prior to the measurement campaign using an Alicona optical profilometer. Surface topologies of these sandpapers are shown in figure 1(b, c), while the key surface parameters in table 3. The test surfaces are subjected to a range of M ($0.3 \leq M \leq 2.9$) and friction Reynolds numbers ($4355 \leq Re_\tau = \delta U_\tau/\nu_w \leq 30292$), where δ is the 99% boundary-layer thickness for each test case at the measurement location, and ν_w is the kinematic viscosity of air at the wall. At a constant $M = 2$, Re_τ sweep is achieved by varying the tunnel's stagnation pressure P_0 from 2.5 to 4.5 bar (table 2). For analyses in this study, profiles are extracted at $x = 29\delta_0$ from the leading edge of the plate for SW and P24 test cases (station '**A**' in figure 1a). Due to a wall reflection issue in the PIV images, the profiles of P60 test cases are extracted from station '**B**', 10 mm downstream of **A** (figure 1a).

Non-time-resolved planar 2D2C particle image velocimetry (PIV) measurements are conducted on the streamwise–wall-normal (x–y) plane, as shown in figure 1(a). The $7.8\delta_0 \times 2.3\delta_0$ (x–y) field-of-view (FOV) is stitched from two 5.5 MP LaVision Imager sCMOS cameras. As many as 400 image pairs are acquired for each test case shown in table 2, with $t^+ = \Delta t U_\tau^2/\nu_w = 2.8$ and the boundary-layer turnover rate of $T_s U_\infty/\delta_0 = 723$ for the reference test case (SW at $M = 0.3$), where Δt is the acquisition interval between a pair of PIV images and T_s is the sampling interval between two subsequent PIV image pairs. PIV cross-correlation is performed using an in-house PIV package developed at the University of Southampton [21], with the final spatial resolution of $\Delta x^+ = \Delta y^+ = 134$ for the reference test case.

2.2 Temperature profiles

As temperature profiles of the developing TBLs and the wall temperatures are not measured in the experiments, these quantities are inferred from the velocity profiles instead. Based on similar studies (compressible, rough-wall TBLs) conducted in similar test facilities (intermittent, blow-down wind tunnels [10, 12, 17]), zero-pressure gradient, $Pr \neq 1$ TBL development over an adiabatic wall is assumed (Pr is the Prandtl number). Using this assumption, the wall temperature T_w is equal to the recovery temperature

T_r and the temperature-velocity profile has a quadratic relation [22, 23] given by,

$$T_w = T_r = T_\infty \left(1 + r\frac{\gamma - 1}{2} M_\infty^2\right) \tag{4}$$

$$\frac{T}{T_\infty} = 1 + r\frac{\gamma - 1}{2} M_\infty^2 \left[1 - \left(\frac{U}{U_\infty}\right)^2\right] \tag{5}$$

where the recovery factor $r = Pr^{1/3}$ [24]. Figure 2 shows the temperature profiles T/T_w as a function of the wall locations y/δ for all test cases. Here, the temperature profile is estimated from the velocity profile from PIV measurements via equation 5, resulting in a decrease in the static temperature towards the edge of the boundary layer as M increases. In the subsonic ($M = 0.3$) cases, the freestream temperature is 1% lower than the wall temperature $T_\infty/T_w = 0.99$. This further decreases by 10% in the transonic cases ($T_\infty/T_w = 0.9$), and in the supersonic cases ($M = 2$ and 2.9), $T_\infty/T_w = 0.6$ and 0.4, respectively.

To obtain the transformed velocity and wall-normal coordinate U_I and y_I in table 1, the density and viscosity profiles relative to the wall, $\rho^+ = \rho/\rho_w$ and $\mu^+ = \mu/\mu_w$, are derived from the temperature profile T/T_w using the boundary layer relation $\partial P/\partial y = 0$ and Sutherland's formula,

$$\rho^+ = \frac{\rho}{\rho_w} = \left(\frac{T}{T_w}\right)^{-1} \quad \text{and} \quad \mu^+ = \frac{\mu}{\mu_w} = \left(\frac{T}{T_w}\right)^{1.5} \left(\frac{T_w + S}{T + S}\right) \tag{6}$$

where $S = 110.4$ K.

2.3 Wall shear stress estimation

Similar to the temperature profiles and wall temperatures, the wall shear stress (WSS) is not directly measured in the experiment. For all test cases (SW, P60, and P24), modified Clauser method [25] is employed. For SW test cases, the method searches for a series of variables (U_τ, ε), where ε is a small wall correction in the $O(0.1$ mm), to minimise the r.m.s. (root mean square) error of

$$\Psi_{smooth} = U_I^+ - \left[\frac{1}{\kappa} \log\left(\frac{(y + \varepsilon)_I U_\tau}{\nu_w}\right) + B\right] \tag{7}$$

in the log region $30 \leq (y + \varepsilon)_I^+ \leq 0.15 Re_{\tau_I}$, where $Re_{\tau_I} = \delta_I U_\tau/\nu_w$.

For P60 and P24 cases, there are two additional variables: the zero plane displacement d and ΔU_I^+ (equation 1). Similar to the approach by [3, 4] for sandpaper roughness, as well as [9] for cube roughness, d is kept constant at $d = -k/2$, where k is physical roughness height determined through surface scanning (see table 3). For this study, we utilise the sandpaper grain reflection on the PIV images to determine the wall location and its downward shift by $k/2$. The final series of variables is $(U_\tau, \varepsilon, \Delta U_I^+)$ that minimise the r.m.s. error of

$$\Psi_{rough} = U_I^+ - \left[\frac{1}{\kappa} \log\left(\frac{(y - k/2 + \varepsilon)_I U_\tau}{\nu_w}\right) + B - \Delta U_I^+\right] \tag{8}$$

within the inertial range $3\sqrt{Re_{\tau_I}} \leq (y - k/2 + \varepsilon)_I^+ \leq 0.15 Re_{\tau_I}$ [3, 4]. To minimise the uncertainty, ε is only fitted for profiles stretched by the Van Driest ('VD') transformation [5], where $y = y_I$ (see table 1). This wall correction ε_{VD} is then applied to the profiles before stretching them with other transformations listed in table 1, and the wall location is not corrected further in the Clauser fitting.

3 Results and discussion

The equivalent sand grain roughness k_s is determined from the fitted ΔU_I^+ (see §2.3) for the incompressible cases at $M = 0.3$. For P60 and P24 roughness at this Mach number, $\Delta U_I^+ > 8$ and thus these cases are within the fully rough regime. The incompressible k_s is derived directly from equation 2, yielding $k_s = 0.531$ and 1.742 mm for P60 and P24 roughness, respectively. Throughout this study, 'k_s' refers to these values, obtained from the incompressible cases at $M = 0.3$.

Figure 3(a) shows the fitted ΔU_I^+ for all test cases in table 2 as a function of k_s^+. Results show that all cases are within the fully rough regime and ΔU_I^+ is relatively independent of the transformations to account for the compressibility effect shown in table 1. There seems to be a proportional relation between M and the log-law intercept, possibly related to the wave drag generated by protrusion of the roughness elements. Here, the subsonic and transonic test cases ($M = 0.3$ and 0.8) follow the log relation (equation

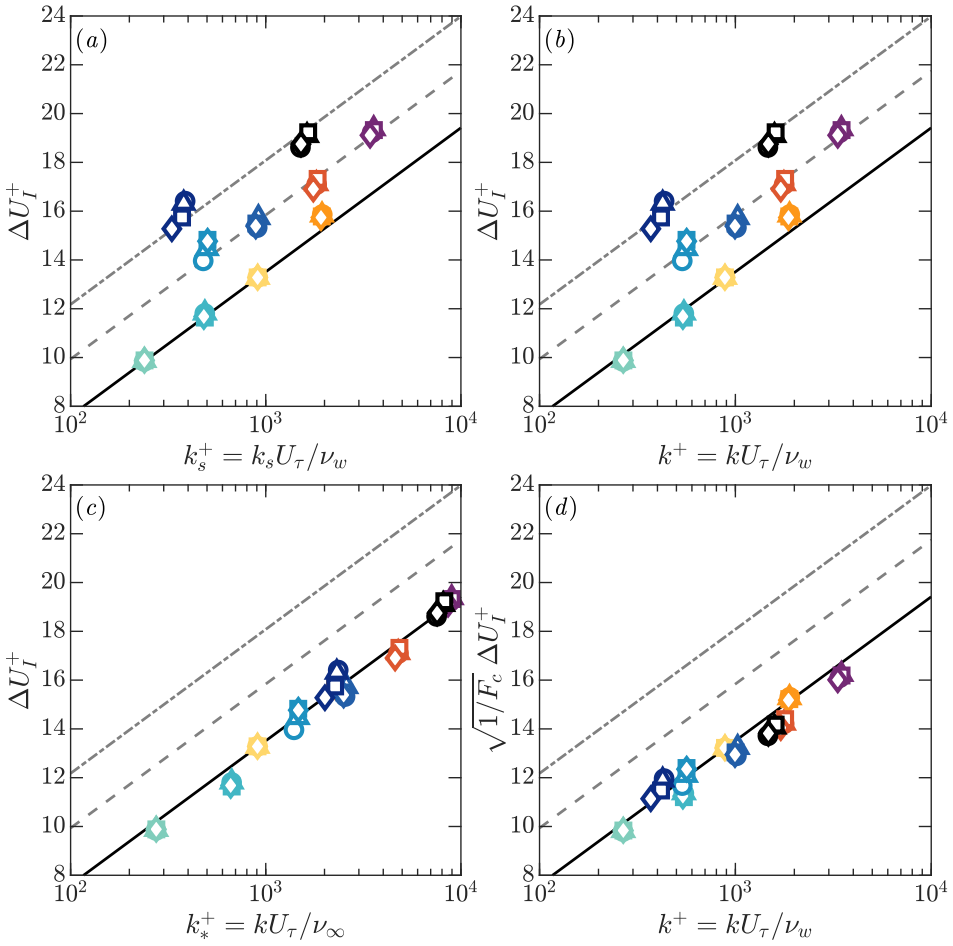


Figure 3: Hama roughness functions obtained from transformed profiles ΔU_I^+ as a function of: (a) the equivalent sand grain roughness from $M = 0.3$ cases, $k_s^+ = k_s U_\tau/\nu_w$, (b) the roughness height $k^+ = kU_\tau/\nu_w$, (c) $k_* = k/\nu_\infty^+$, and $k_*^+ = kU_\tau/\nu_\infty$. (d) The transformed Hama roughnes function ΔU_I^+ multiplied by $\sqrt{1/F_c}$. Lines correspond to the log relations for $M < 1$, $1/\kappa \log k_s^+ + B - B_{FR}$ (——), $M = 2$ (- - -), and $M = 2.9$ (- · - ·). Symbols correspond to various transformations listed in table 1, while the colours correspond to the test cases listed in table 2.

2), while the intercept $B - B_{FR}$ seem to increase with M for the supersonic cases ($M = 2$ and 2.9). These observations still hold if the physical roughness height k is utilised instead of k_s, as shown in figure 3(b), similar to a study in cube roughness by [9]. It should be noted, however, that direct wall shear stress measurements are not conducted in this study, and the ΔU_I^+ in figure 3(a) is obtained from a log-law fitting described in §2.3.

Observing figures 3(a, b), it is apparent that in order to utilise the incompressible flow framework for drag estimation (equation 2), either k_s (or k), i.e. the x-axis, or the ΔU_I^+ (y-axis) must be scaled by a factor to account for the wave drag effect. In figure 3(c), a new roughness lengthscale, defined by $k_* = k/\nu_\infty^+ = k\nu_w/\nu_\infty$, is introduced. Using this empirical lengthscale, the ΔU_I^+ of all test cases collapse to the log relation (equation 2). It should be noted that similar empirical lengthscales have been suggested in previous studies: $k_* = k/\nu_k^+$ for cube roughness [9] and $k_*^+ = k/\nu_k\sqrt{\tau_w/\rho_k}$ for traverse bars and cubes [26], where subscript 'k' denotes flow properties at the tip of the cube. Present data for sandpaper roughnesses, however, does not collapse to the log relation using these lengthscales.

Another possible correction factor is one developed for $C_f = 2(\rho_w/\rho_\infty)(U_\tau/U_\infty)^2$ in compressible SW

TBLs. Derivation of the velocity profile transformed using VD [5] yields a correction factor F_c [27],

$$F_c = \frac{T_w/T_\infty - 1}{\arcsin^2(\alpha)}, \quad \text{where} \quad \alpha = \frac{T_w/T_\infty - 1}{\sqrt{T_w/T_\infty(T_w/T_\infty - 1)}} \tag{9}$$

that collapses the corrected skin friction $F_c C_f$ to the Schlichting's fit [28] for compressible SW TBLs. The same correction factor is calculated for rough wall cases and appropriately scaled for ΔU_I^+, $\sqrt{1/F_c}\Delta U_I^+$. Figure 3(d) shows $\sqrt{1/F_c}\Delta U_I^+$ as a function of k^+, with all test cases collapsing to the log relation (equation 2). It should be noted that, similar to the k_* lengthscale in figure 1(c), the scaling factor F_c is of an empirical nature: it was derived based on the VD-transformed velocity profiles for smooth wall TBLs, rather than various rough wall cases with multiple velocity transformations, as is the case in this study.

4 Conclusion and future work

Experiments are conducted for TBLs developing over two types of sandpaper rough walls (P60- and P24-grit), spanning both incompressible and compressible flow regime ($0.3 \leq M \leq 2.9$) with an independent variation of Re_τ at a constant M. Results suggest that the momentum deficit ΔU_I^+ is relatively independent of transformations to account for compressibility effects and the log relation intercept $B - B_{FR}$ (equation 2) in the compressible flow regime seems to be proportional to M. To be able to utilise the log relation, two scaling factors are introduced. The first is a roughness lengthscale $k_* = k/\nu_\infty^+$ and the second is a correction factor for C_f, here utilised for the roughness function $\sqrt{1/F_c}\Delta U_I^+$. It should be noted that these correction factors are obtained empirically and they have not been validated for other roughness data. Furthermore, we cannot rule out that these observations may be caused by a systematic change in our experiment as the Mach number is changed. In the future, the derivation of the theoretical correction factor from the roughness function, accounting for the appropriate incompressible flow analogies, as well as the validation of these scaling factors with other available roughness data should follow.

References

[1] F. R. Hama. Boundary layer characteristics for smooth and rough surfaces. *Trans. Soc. Nav. Arch. Marine Engrs.*, 62:333–351, 1954.

[2] J. Nikuradse. Laws of flow in rough pipes. *NACA Tech. Mem.*, 1292, 1933.

[3] D. T. Squire, C. Morrill-Winter, N. Hutchins, M. P. Schultz, J. C. Klewicki, and I. Marusic. Comparison of turbulent boundary layers over smooth and rough surfaces up to high reynolds numbers. *J. Fluid Mech.*, 795:210–240, 2016.

[4] M. Gul and B. Ganapathisubramani. Revisiting rough-wall turbulent boundary layers over sand-grain roughness. *J. Fluid Mech.*, 911:A26, 2021.

[5] E. R. van Driest. Turbulent boundary layer in compressible fluids. *J. Aeronaut. Sci.*, 18:1012, 1951.

[6] C. Brun, M. P. Boiarciuc, M. Haberkorn, and P. Comte. Large eddy simulation of compressible channel flow: Arguments in favour of universality of compressible turbulent wall bounded flows. *Theor. Comput. Fluid Dyn.*, 22:189–212, 2008.

[7] A. Trettel and J. Larsson. Mean velocity scaling for compressible wall turbulence with heat transfer. *Phys. Fluids*, 28:026102, 2016.

[8] P. S. Volpiani, P. S. Iyer, S. Pirozzoli, and J. Larsson. Data-driven compressibility transformation for turbulent wall layers. *Phys. Rev. Fluids*, 5:052602(R), 2020.

[9] D. Modesti, S. Sathyanarayana, F. Salvadore, and M. Bernardini. Direct numerical simulation of supersonic turbulent flows over rough surfaces. *J. Fluid Mech.*, 942:A44, 2022.

[10] F. E. Goddard. Effect of uniformly distributed roughness on trubulent skin-friction drag at supersonic speeds. *J. Aerosp. Sci.*, 26(1):1–15, 1959.

[11] D. C. Reda, F. C. Ketter, and C. Fan. Compressible turbulent skin friction on rough and rough/wavy walls. *AIAA J.*, 13(5):553–554, 1975.

[12] R. M. Latin and R. D. W. Bowersox. Flow properties of a supersonic turbulent boundary layer with wall roughness. *AIAA J.*, 38(10):1804–1821, 2000.

[13] D. E. Berg. Surface roughness effects on a mach 6 turbulent boundary layer. *AIAA J.*, 17(9):929–930, 1979.

[14] D. Sahoo, M. Schultze, and A. Smits. Effects of roughness on a turbulent boundary layer in hypersonic flow. In *Proceedings of the 39th AIAA Fluid Dynamics Conference*, pages AIAA 2009–3678. American Institute of Aeronautics and Astronautics, 2009.

[15] C. J. Tyson and N. D. Sandham. Numerical simulation of fully-developed compressible flows over wavy surfaces. *Int. J. Heat Fluid Flow*, 41:2–15, 2013.

[16] M. Aghaei-Jouybari, J. Yuan, Z. Li, G. J. Brereton, and F. A. Jaberi. Supersonic turbulent flows over sinusoidal rough walls. *J. Fluid Mech.*, 956:A3, 2023.

[17] I. W. Ekoto, R. D. W. Bowersox, T. Beutner, and L. Goss. Supersonic boundary layers with periodic surface roughness. *AIAA J.*, 46(2):487–497, 2008.

[18] D. Neeb, P. Marquardt, and A. Gülhan. Characterization of a hypersonic turbulent boundary layer along a sharp cone with smooth and transverse squarebar roughened wall. *Exp. Fluids*, 65:144, 2024.

[19] Y. Wang and Z. Gao. Roughness effects on compressible turbulent boundary layers under different mach numbers and wall temperature conditions. *Phys. Fluids*, 36:025144, 2024.

[20] S. J. Peltier, R. A. Humble, and R. D. W. Bowersox. Crosshatch roughness distortions on a hypersonic turbulent boundary layer. *Phys. Fluids*, 28:045105, 2016.

[21] J. M. Lawson. *A scanning PIV study of homogeneous turbulence at the dissipation scale*. Phd thesis, University of Cambridge, 2016. Code repository at https://git.soton.ac.uk/jml1g18/pivtools.

[22] L. Crocco. The laminar boundary layer in gases. Technical report, North American Aviation, Aerophysics Laboratory, 1948.

[23] E. R. van Driest. *The turbulent boundary layer with variable Prandtl number*. Vieweg+Teubner Verlag, 1955.

[24] S. Pirozzoli and M. Bernardini. Turbulence in supersonic boundary layers at moderate reynolds number. *J. Fluid Mech.*, 688:120–168, 2011.

[25] F. H. Clauser. Turbulent boundary layers in adverse pressure gradients. *J. Aero. Sci.*, 21(2):91–108, 1954.

[26] D. Neeb, A. Gülhan, and J. A. Merrifield. Rough-wall heat flux augmentation analysiswithin the exomars project. *J. Spacecr. Rockets*, 53(1):121–133, 2016.

[27] E. J. Hopkins and M. Inouye. An evaluation of theories for predicting turbulent skin friction and heat transfer on flat plates at supersonic and hypersonic mach numbers. *AIAA J.*, 9(6):993–1003, 1971.

[28] H. Schlichting and K. Gersten. *Boundary-Layer Theory*. McGraw-Hill, New York, 4 edition, 1960.